

# A First Analysis of JET Plasma Profile-Based Indicators for Disruption Prediction and Avoidance

A. Pau<sup>1</sup>, A. Fanni, B. Cannas, S. Carcangiu, G. Pisano, G. Sias, P. Sparapani, M. Baruzzo, A. Murari, F. Rimini, M. Tsalas, P. C. de Vries, and the JET Contributors\*

**Abstract**—Reliable algorithms for disruption avoidance and prediction are foreseen to play a fundamental role in the JET control system for the successful operation of the machine in the upcoming deuterium-tritium campaigns. The integration of such algorithms is expected to be a key part also in the implementation of the ITER plasma control system. So far, most of the effort has been devoted to the prediction of disruptions, which is required to mitigate the effects of these transient events, protecting the integrity of in-vessel components. Nevertheless, in order to put in place recover strategies or to have the possibility of a soft landing for the plasma current, the paradigm must be shifted to avoiding disruptions. In this paper, plasma profile-based indicators will be statistically analyzed showing their potential in such a perspective, where warning times and reliability of detection are crucial.

**Index Terms**—Disruption avoidance, disruption prediction, operational space mapping, plasma profiles.

## I. INTRODUCTION

DISRUPTIVE events still pose a serious problem for the operation of large size tokamak devices, representing, therefore, a key aspect to be considered for the design and operational strategies of next step fusion devices such as ITER and DEMO [1]. If an efficient mitigation is required to avoid damage to the machine, efficient avoidance schemes are needed to possibly bring the plasma back to a nondisruptive operating condition. The better the avoidance schemes (i.e., lower risk of a disruption), the lower is the performance

requirements for the mitigation schemes [2]. In this framework, disruption prediction plays a key role and in the last few years, a substantial effort has been devoted to developing more sophisticated prediction systems and improving their performance both in terms of success rate and warning time [3]–[6]. Many of the presently developed disruption predictors mainly rely on magnetohydrodynamic (MHD) markers related to still rotating modes and, especially, to locked modes, which are basically the final precursor of most of the disruptions. Nevertheless, in many cases, the warning time is still unsatisfactory with respect to avoidance requirements, and a significant step forward needs to be taken.

This paper deals with the development of “plasma profile-based indicators” for disruption prediction and avoidance in JET, where parameterized peaking factors (PFs) have been implemented for electron temperature, density, and plasma radiation profiles. Profile-based indicators are important because of their close connection with the plasma stability and the destabilization of MHD modes that eventually cause the disruption. The basic interplay of the time evolution of different profiles will be described in relation to the phenomenology characterizing specific disruption types together with the relevant time scales. Furthermore, a statistical analysis aiming to describe differences and boundaries between the nondisruptive and the disruptive space as well as among specific types of disruptions will be presented, discussing the implications in terms of disruption prediction and avoidance.

## II. PEAKING FACTORS

In [3]–[7], several physics and engineering parameters have been considered both for disruption prediction and classification purposes, but many of them depend significantly on specific machine configurations or characteristics, and on the scientific program carried out throughout the experimental campaigns. As known, the performance of machine learning algorithms deteriorates outside the training domain and this poses serious concerns in terms of extrapolation to the next step fusion devices. That is why it is very important to focus the attention on something more invariant with respect to the operational domain than the engineering parameters traditionally used. For this purpose, some physics-based indicators have been synthesized, which contain information on the time evolution of the main plasma profiles such as the electron temperature, the radiated power, and the electron density. In fact, in many cases, the information contained in the profiles is strongly related to the phenomenology that

Manuscript received June 30, 2017; revised February 12, 2018; accepted April 6, 2018. Date of publication June 12, 2018; date of current version July 9, 2018. This work was supported by the Euratom Research and Training Program 2014–2018 under Grant 633053. The review of this paper was arranged by Senior Editor E. Surrey. \*See the author list of “Overview of the JET results in support to ITER” by X. Litaudon *et al.* to be published in Nuclear Fusion Special issue: overview and summary reports from the 26th Fusion Energy Conference (Kyoto, Japan, 17–22 October 2016). (Corresponding author: A. Pau.)

A. Pau, A. Fanni, B. Cannas, S. Carcangiu, G. Pisano, G. Sias, and P. Sparapani are with the Electrical and Electronic Engineering Department, University of Cagliari, 09123 Cagliari, Italy (e-mail: alessandro.pau@diee.unica.it).

M. Baruzzo and A. Murari are with the Consorzio RFX (CNR, ENEA, INFN, Università di Padova, Acciaierie Venete SpA), Corso Stati Uniti 4, 35127 Padova, Italy.

F. Rimini is with the CCFE, Culham Science Center, OX14 3DB Abingdon, U.K.

M. Tsalas and P. C. de Vries are with ITER Organization, 13067 Saint-Paul-lès-Durance, France.

EUROfusion Consortium, JET, Culham Science Centre, Abingdon, OX14 3DB, U.K.

Color versions of one or more of the figures in this paper are available online at <http://ieeexplore.ieee.org>.

Digital Object Identifier 10.1109/TPS.2018.2841394

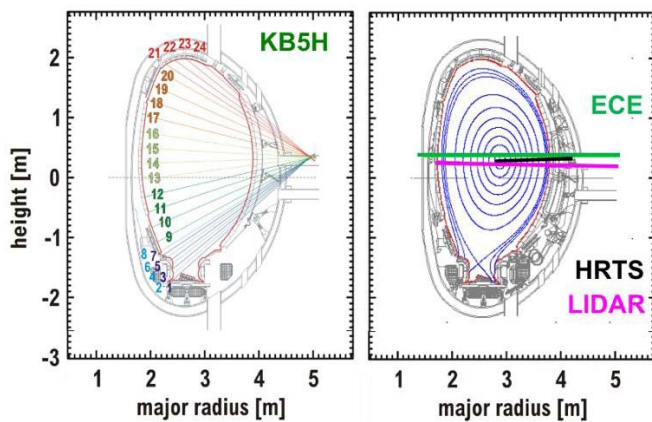


Fig. 1. Horizontal view bolometer KB5H at JET (left) and line of sight in the poloidal section for ECE, HRTS, and LIDAR diagnostics (right).

characterizes different disruptive processes. In this paper, PFs, indicative of the radial profile of the aforementioned plasma parameters, have been considered as a feature to study the interaction of their time evolution during the chain of events leading to disruption.

To calculate the peaking of the profiles for the electron temperature, the electron cyclotron emission (ECE) or the high-resolution Thomson scattering (HRTS) diagnostics have been considered. JET ECE heterodyne radiometer consists of 96 channels over four data acquisition bands, allowing either the first-harmonic measurements (O-mode) or the second-harmonic measurements (X-mode). HRTS diagnostic at JET measures electron temperature ( $T_e$ ) and electron density ( $N_e$ ), providing 63 data points per profile with a repetition rate of 20 light pulses per second (20 Hz). The spatial resolution of the measurements for the core region and the pedestal is, respectively, of 1.6 and 1 cm. As the HRTS is not guaranteed to be available in real time for the next campaigns at JET, it has been used mainly to check the consistency of the ECE measurements and, in the few cases, where ECE was not available, to replace it for the PF calculation. Concerning the radiated power, the main-vessel bolometric cameras with horizontal views of the plasma cross section (KB5H) have been used. The camera collects the radiation along 24 chords, eight of which cross the divertor region and the region adjacent to the divertor with 8-cm separation between the chord axes. The other 16 channels cover the entire plasma [see Fig. 1 (left)]. A simple pinhole structure is used to define the lines-of-sight of the camera [8].

Regarding the electron density profiles, the data coming from the density profile reflectometry system (33–160 GHz) at JET have been analyzed because of their availability in real time. Unfortunately, because of a significant number of channels in cutoff, the coverage of the radial interval of interest turned out to be not adequate for many disruptive pulses of the considered database. Therefore, to synthesize an indicator representative of the electron density profile, again the HRTS diagnostic has been used. Another diagnostic providing kinetic profiles at JET is the laser imaging detection and ranging (LIDAR), an incoherent Thomson scattering which measures

local electron temperature and density along a horizontal almost midplane line of sight. With a repetition rate of 4 Hz and a spatial resolution of approximately 12 cm, such a diagnostic is able to provide a coverage of almost the entire plasma cross section. LIDAR data have not been used for the analyses described in this paper, but the diagnostic has been taken into account for data consistency evaluation.

Each PF is a “core versus all” metric, i.e., it is defined as the ratio between the mean value of the considered radial profile (temperature, radiation, and density) around the magnetic axis and the mean value of the measures on the entire radius. The radial interval to define the “core” has been empirically set equal to 10% of the radial axis (the minor radius for the horizontal midplane measurements and the vertical semiaxis of the poloidal cross section for the horizontal bolometer camera measurements). The value of 10% has been selected as a good compromise for having a reasonable number of measurements to define the core (guaranteeing in this way a more robust estimation) in a radial interval where the gradient is not changing too much. Other definitions could be adopted, and different meanings could be attributed to “PFs” depending on the specific analysis; in this paper, the aim is to define a statistically robust parameter, whose definition can be conceptually applied to different profiles and generalized for different machines. A more detailed discussion about the implications of this definition in relation to specific physics behaviors or phenomena is out of the scope of this paper.

Fig. 2 shows the time evolution of the radial profiles for the aforementioned plasma parameters with, in addition, the internal inductance, representative of the peaking of the plasma current density, for a disruption due to tungsten (W) accumulation in the plasma core. In the following, we will make reference to this type of disruption characterized by core radiative collapse as CoreRC.

The typical process with which high-Z impurities degrade the energy confinement, leading not rarely to disruption, is well known and it has been described in [7]. As the sawtooth activity stops and the accumulation of W in the plasma core starts to build up, both radiation and electron density peak. On the contrary, because of the strong radiation from the plasma core [Fig. 2(c)], the electron temperature profile flattens or even hollows depending on the plasma underlying conditions. This, in turn, gives rise to a corresponding broadening of the current density profile, as can be seen from the time evolution of the internal inductance [Fig. 2(a)], which keeps reducing up to the final locked mode, eventually triggering the disruption. Note that the time evolution of the  $T_e$  PF from the ECE diagnostic can be affected by channels in cutoff for a specific radial location, which happens for relatively high-density and low-field plasmas. As shown in Fig. 2(b), after ~49 s, a cutoff affecting the edge channels and propagating inward translates into a slight peaking of the considered indicator. This behavior, in fact, is not in agreement with the PF calculated from HRTS data, whose time evolution is roughly constant until the strong increase in the core radiation. This condition must be avoided and properly detected during real-time monitoring, and to this aim, specific algorithms based on the cross correlation

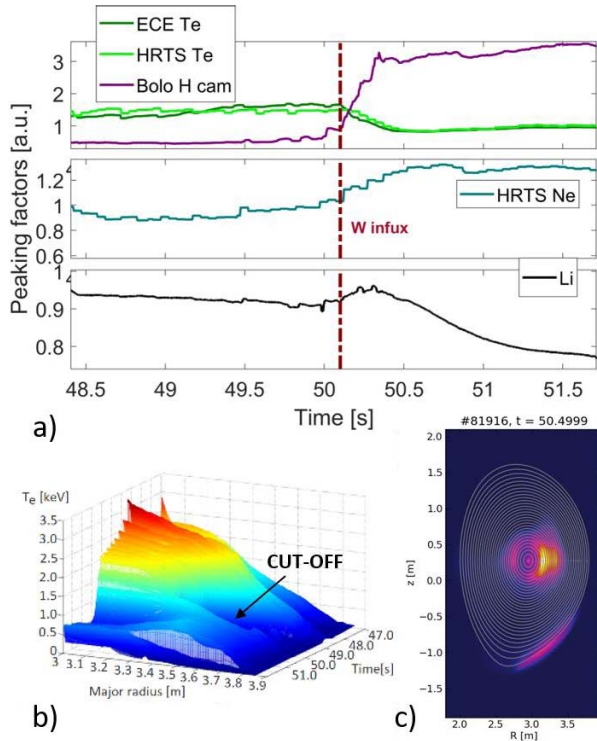


Fig. 2. (a) Time evolution of the PFs [a.u.], respectively, for  $T_e$  from ECE and HRTS measurements and for the radiation from the horizontal bolometer camera, PF time evolution for the electron density ( $N_e$ ) from the HRTS diagnostic, internal inductance (top–bottom). (b) 3-D spatial distribution from ECE diagnostic. (c) 2-D distribution of the radiation from horizontal (KB5H) and vertical bolometer (KB5V) cameras.

of the measurements for different channels are being developed. In the database considered for this analysis, CoreRC disruptions represent more than 60% of the total cases. Such disruption class is of paramount importance not only because of its strong impact on JET operations, but also because of its direct connection to the ITER-like wall (ILW) materials.

Fig. 3, conversely, shows a completely different behavior of the time evolution of the considered plasma profiles. The discharge was aimed to pellet edge localised mode pacing studies and a problem on the density control triggered a disruption with a multifaceted asymmetric radiation from the edge (MARFE) developing at about 57 s. The corresponding large increase of the edge density gave rise to the radiative collapse eventually degrading the plasma up to the final locked mode. This is very well described by the interplay of the PFs' time evolution [Fig. 3(a)]. The edge radiative collapse is synthesized by the peaking of the  $T_e$  profile, whose evolution is anticorrelated with respect to the variation of the electron density profile. It is very important to note that this behavior is building up in a condition of divertor dominated radiation and a slow progressive contraction of the plasma current profile. In the following, we will refer to this type of disruption as EdgeRC.

Therefore, basically, there are two components that play a role: the combination of the time evolution of the main plasma profiles and the plasma underlying conditions where the relevant phenomenology takes place. These mechanisms are

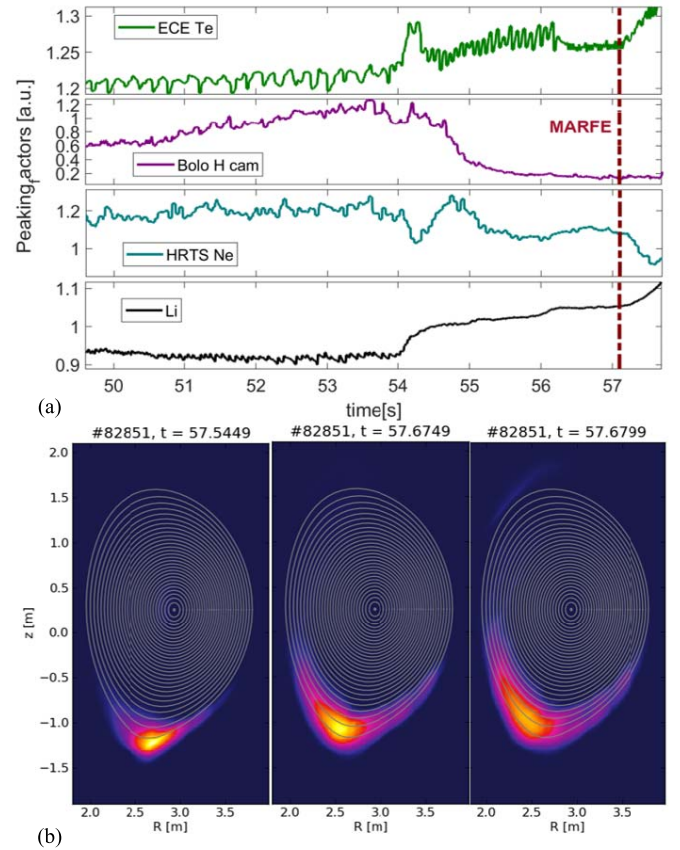


Fig. 3. Density control problem disruption. (a) Time evolution of the PFs [a.u.], respectively, for  $T_e$  from ECE, radiation from the horizontal bolometer camera, electron density ( $N_e$ ) from the HRTS diagnostic, internal inductance (top–bottom). (b) 2-D distribution of the radiation from horizontal (KB5H) and vertical bolometer (KB5V) cameras for three different time instants showing MARFE development.

strictly connected to the MHD stability; indeed, most of the time, the locked mode is the final precursor leading to disruption. Very often, the change in the profile time evolution takes place over much longer time scales, and this is extremely important for the avoidance requirements. Another third important ingredient needs to be taken into account: the robustness in the identification of boundaries and conditions leading with high probability to disruption. This aspect will be addressed in Section III describing the univariate statistical distributions of different PFs.

### III. UNIVARIATE STATISTICAL ANALYSIS

A univariate statistical analysis has been performed in order to evaluate the power of each PF both in discriminating between disruptive and nondisruptive behavior and among different types of disruptions. To this end, different scenarios have been considered, as described in the following section. Note that in this univariate analysis, no combination among the features has been considered, which would greatly increase the discrimination and prediction capability of the plasma profiles, as will be discussed in Section IV. The statistical analyses have been performed referring to a database of 149 nonintentional disruptions, already considered in [7], and 126 nondisrupted



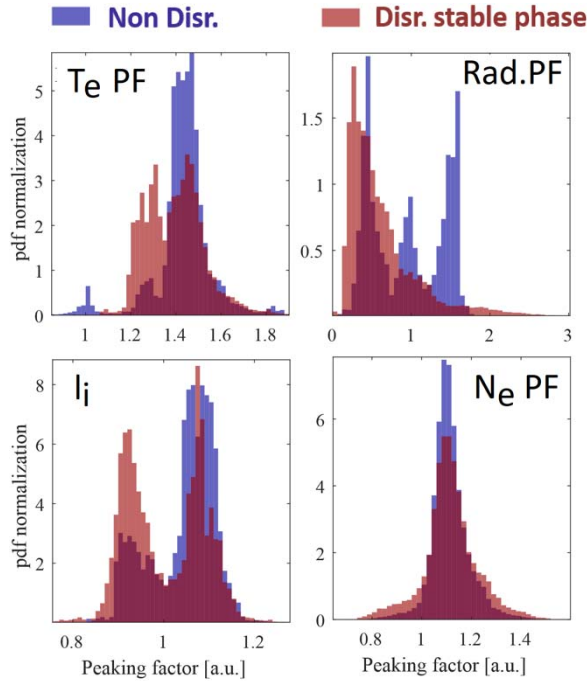


Fig. 4. Probability distribution functions of the PFs of the nondisruptive pulses (blue) versus the stable phase of the disruptive pulses (red) for electron temperature, radiated power, current density (internal inductance), and electron density (from top left to bottom right).

pulses that occurred between 2011 and 2013. The nondisruptive pulses were selected trying to preserve as much as possible the “variability” of the nondisruptive population together with plasma scenarios and experiments which the disruptive population belongs to. For the considered disruptions, the manual classification, already available [9], [10], has been further detailed analyzing different time intervals of the main events characterizing the disruptive process. For a few tens of these pulses, the diagnostic signals were not available or corrupted, and consequently have been discarded. Hence, the final database analyzed in this paper is composed of 135 disrupted and 120 nondisrupted discharges. For each disruptive shot, a “stable phase” is defined as the plasma current flat top till the point where the plasma is definitely destabilized, that is, in correspondence of the start of the chain of events leading to disruption from which the plasma does not recover anymore. This point corresponds to the onset of the “unstable” phase too, which lasts up to the disruption or to the final precursor to disruption (large thermal quench or locked mode), which changes dramatically the time evolution of the profiles, making, in the framework of this analysis, meaningless the related information content.

#### A. Disrupted Versus Nondisrupted Discharges

The first scenario considers the stable phase of the disrupted discharges versus all the flat top of the nondisrupted ones, regardless of the disruption type. Hence, both classes refer to phases in which the plasma can be considered in a stable condition.

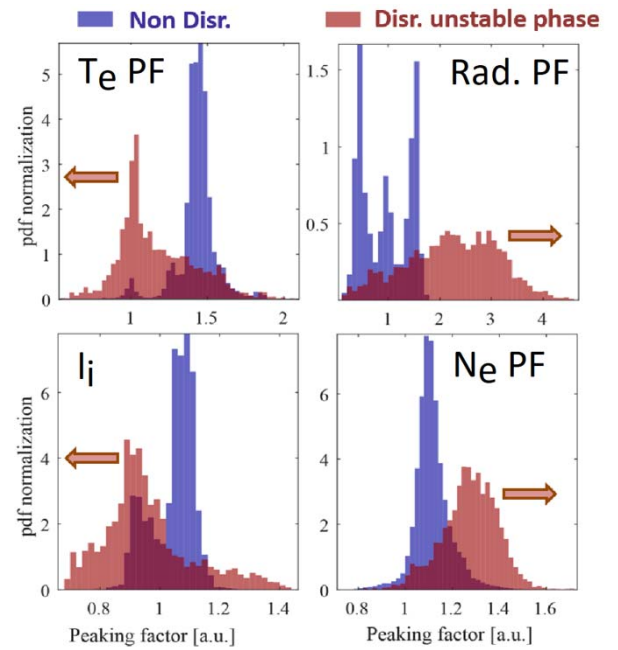


Fig. 5. Probability distribution functions of the PFs of the nondisruptive pulses (blue) versus the unstable phase of the disruptive pulses (red) for electron temperature, radiated power, current density (internal inductance), and electron density (from top left to bottom right).

In Fig. 4, the histograms of the samples coming from the flat top of the nondisrupted pulses (blue) and from the stable phase of the disruptive pulses (red) are reported for the PFs of the three considered profiles, namely, the electron temperature, the radiated power, and the electron density, together with the internal inductance, that is, itself an indicator of the peaking of the current density profile. These histograms have been normalized providing the probability density functions (pdf) and considering the same bin width for both the distributions, so that the ratio of overlapping bins gives directly the proportion in terms of probability. As can be seen, except for the electron density, the distributions are quite different. Referring, as an example, to the temperature PF ( $T_e$ PF), the ranges of variation of the two distributions are comparable but the nondisruptive pulses have a unimodal distribution, with the maximum value corresponding to a PF between 1.4 and 1.6, whereas the stable phase of the disruptive population is characterized by a bimodal distribution.

Referring to the radiation peaking, the nondisruptive discharges present a trimodal distribution probably due to the presence, in the selected database, of a wide range of plasma scenarios and operating conditions, as expected in an experimental machine. Nevertheless, no one of the considered conditions resulted in a radiation PF (Rad.PF) greater than 1.7, which can be assumed as a sort of empirical higher bound for the nondisrupted discharges.

The second scenario refers to the unstable phase of the disrupted pulses versus all the flat top of the nondisrupted shots. Fig. 5 reports the pdfs of the nondisrupted pulses (blue) and of the unstable phase of the disruptive pulses (red) for the PFs of the electron temperature, the radiated power, the electron density, and the internal inductance.

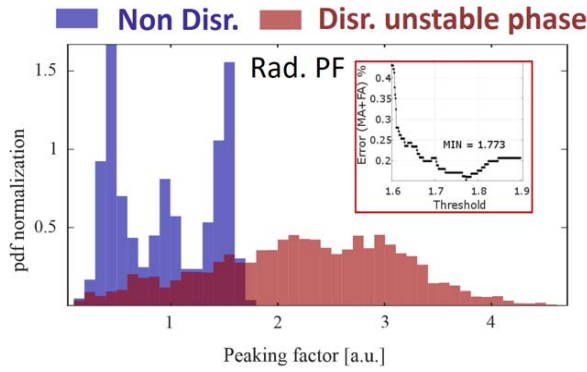


Fig. 6. Selection of the thresholds for the radiation peaking disruption predictor. In the framework, the trend of the prediction errors (MAs + FAs) with threshold, where MAs are the fraction of disruptive discharges predicted as nondisruptive, whereas FAs are defined as the fraction of nondisruptive discharges predicted as disruptive.

As can be observed, basically for all the considered parameters, the overlapping area dramatically reduced with respect to the previous analyzed scenario highlighting the potential of the introduced indicators to distinguish between disrupted and nondisrupted behaviors. In particular, the distribution of the  $T_e$ PF for the phases considered for the disruptive discharges shifts toward lower values, whereas that of the radiation shifts significantly toward higher values. This, as can be easily inferred from the discussion of the examples in Section II, is mainly due to the presence of a large percentage of CoreRC disruptions in the considered database that represents one of the most common causes of disruption at JET after the installation of the ILW.

All the distributions of the PFs in Fig. 5 suggest the possibility to choose suitable thresholds to discriminate between disrupted and nondisrupted behaviors. The discrimination capability between the two considered classes has been evaluated by analyzing the prediction performance obtained applying an optimized threshold to the radiation peaking alone. In this framework, “prediction” is meant as the capability to “detect” a disruptive behavior on the basis of the information carried out by diagnostic data, providing an early indication of impending disruption, so that avoidance and/or pre-emptive mitigation measures can be taken [11].

Different thresholds have been tested. Because of their intrinsic statistical meaning, the thresholds minimizing the overlapping of the two distributions according to the Bayes optimal decision boundary (equal to 1.59), and corresponding to the inversion of the ratio between the two distributions (equal to 1.65) have been considered. Another threshold has been evaluated, minimizing the sum of missed alarms (MAs) and false alarms (FAs), which corresponds to a value of  $\sim 1.77$  (Fig. 6). Table I reports the prediction performance obtained with the selected thresholds. As expected, the optimized threshold performs better if defined in terms of FAs. Note that with such an optimization, among the 20 MAs, only one is due to CoreRC disruptions. This is due to the fact that the main phenomenology characterizing this disruption type is exhaustively described by the time evolution of the considered profile and that the defined PF results to be robust enough to

TABLE I  
DISCRIMINATION CAPABILITY OF RAD.PF IN TERMS OF MAs AND FA

Threshold	Missed Alarms	False Alarms
1.59	17/135 12.59%	41/120 34.17%
1.65	18/135 13.33%	11/120 9.17%
1.77	20/135 14.81%	1/120 0.83%

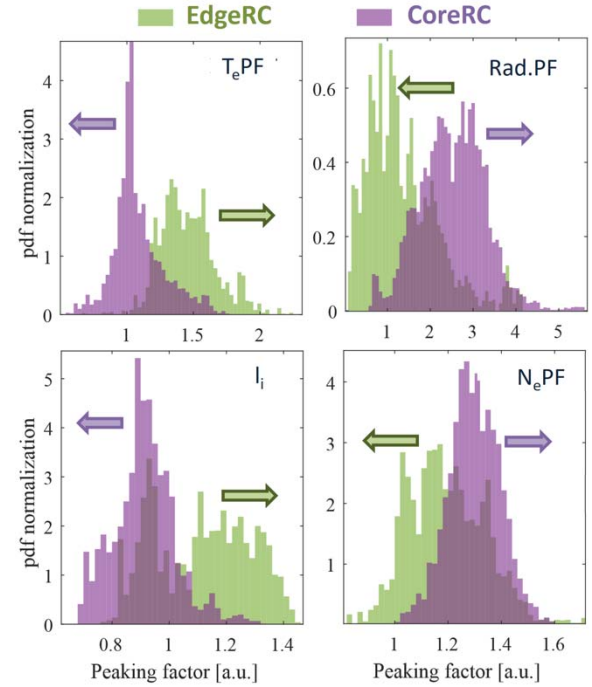


Fig. 7. Probability distribution functions of the PFs of the unstable phase of the CoreRC disruptions (purple) versus the unstable phase of the EdgeRC disruptions (green) of electron temperature, radiated power, internal inductance, and electron density (from top left to bottom right).

catch the changes involved in the unstable phase leading to disruption.

On the other hand, the larger variety of behaviors characterizing the disruption classes collected in the other group (EdgeRC) involves a broader plethora of phenomena where the time evolution of the considered profiles combines in different ways. Hence, it is worth performing a further univariate analysis discriminating between CoreRC and EdgeRC disruptions.

### B. CoreRC Versus EdgeRC Disruptions

The univariate analysis performed on the previously calculated PFs, resulted to be useful also to have a first discrimination among different types of disruptions. In fact, the information contained in the profiles is connected to the phenomenology characterizing different disruptive processes.

Fig. 7 reports the pdfs of the unstable phase of the high-Z impurity accumulation disruptions (CoreRC) (purple) and that of the unstable phase of all the other disruptions (EdgeRC)

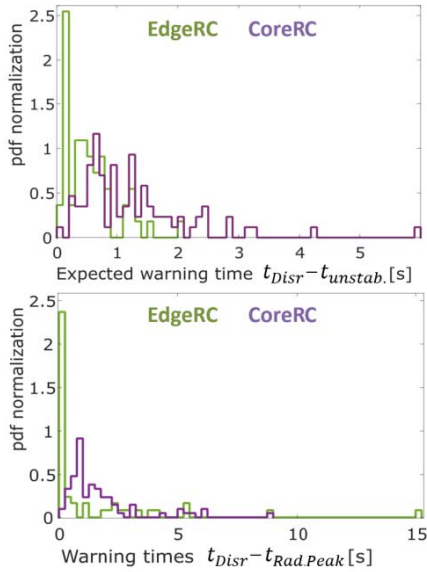


Fig. 8. PDFs of the warning times of CoreRC (purple) versus EdgeRC (green) disruptions. Expected warning times evaluated with respect to the start of the chain of events leading to disruption (top). Actual warning times obtained thresholding the Rad.PF (bottom). (Note that in this case, the threshold obtained by minimizing the sum of MAs and FAs gives rise also to some early detection, associated with warning times higher than those expected and not directly connected to the chain of events leading to disruption.

(green) for the PFs of the electron temperature, the radiated power, the electron density, and the internal inductance.

As in the previous cases, the pdfs of different PFs are quite different comparing the CoreRC disruptions versus all the EdgeRC disruptions. In particular, in the unstable phase, CoreRC disruptions present values of the  $T_e$  PF significantly lower than that of the other disruptions. This is consistent with the phenomenology that characterizes the CoreRC class, namely, flattening or even hollowing of the radial temperature profile.

Conversely, the PFs related to the unstable phase of EdgeRC disruptions have a statistical distribution driven by the cooling radiative collapse at the edge, which is a common feature of the final path of the disruptions grouped in this class. The unfolding of such a phenomenology, as well known, involves the contraction/peaking of the electron temperature and current density profiles, and on the other hand, a strong increase of radiation and density at the edge that reflects in a shift of the distributions toward lower values of the respective PFs. Also in this case, suitable thresholds could be optimized to discriminate among different classes. However, as discussed in Section I, what is really powerful is the information associated with the interplay of the individual profiles, and this will be discussed in Section IV in terms of multidimensional space analysis.

### C. Warning Times

The characterization of the CoreRC versus the EdgeRC disruptions keeps being quite different also considering the warning times obtained by thresholding the single PFs. As an example, Fig. 8 reports the distributions of the expected

warning times, evaluated with respect to the start of the unstable phase  $t_{unstab}$ . [Fig. 8 (top)], and of the actual warning times corresponding to the alarms  $t_{Rad.Peak}$  of a “predictor” obtained by simply thresholding the Rad.PF alone [Fig. 8 (bottom)] for the two analyzed disruptive groups.

As can be seen, by comparing these latter with the expected ones, the warning time distributions are qualitatively similar, especially for the CoreRC disruptions, and confirm the potential of the proposed indicators for avoidance purposes.

## IV. MACHINE LEARNING FOR MULTIDIMENSIONAL ANALYSIS

As well known, disruptions can be due to the nonlinear interaction of many parameters and, depending on the causes and the phenomenology, they can evolve in different regions of the operational space. Recently, an advanced machine learning technique has been successfully exploited to investigate the JET high-dimensional space where the relevant disruption physics takes place [6], [7]. Such a technique, which is the generative topographic mapping (GTM), is a generative model that belongs to the class of the so-called manifold learning techniques. By mapping on a low-dimensional space the complex manifold embedded in the high-dimensional space, the GTM algorithm allows uncovering complex structures, patterns, and operational boundaries described by the complex relation among the parameters in the considered operational space.

The technique performs a nonlinear mapping through radial basis functions (RBFs) from the latent space to the data space, fitting a mixture of Gaussians which are constrained to lie on the low-dimensional space embedded in the original high-dimensional one. Despite the complexity of the model, the concept behind the method is very simple: since the mapping is defined by a smooth and continuous nonlinear function, the topographic ordering and the proximity relations in the latent space are preserved in the original data space, regardless of the dimensionality reduction. In fact, for visualization purposes, the latent space is chosen to be 2-D or 3-D [12]. Fig. 9 reports the GTM scheme for the mapping from the latent space to the data space. In this paper, the GTM tool developed in [13] has been exploited to map a 5-D space including only indicators representative of the radial profiles described in Section II, namely:

- 1)  $T_e$  profile PF from ECE diagnostic;
- 2) radiation profile PF from the horizontal bolometer camera;
- 3) internal inductance  $L_i$  (current density profile PF) from EFIT equilibrium code;
- 4)  $q_{95}/q_0$  ratio from EFIT equilibrium code;
- 5)  $N_e$  profile PF from HRTS diagnostic.

To the set of four parameters already discussed in Sections II and III, the  $q_{95}/q_0$  ratio has been added to investigate possible differences with respect to the information provided by the internal inductance. In Fig. 10, the pieplane representation of the resulting 2-D GTM mapping is shown. Such a mapping has been obtained for a latent square grid of  $45 \times 45$  points, 196 RBF with a width  $\sigma$  of 1.5. Such parameters have been selected as a tradeoff between smoothness and flexibility of the



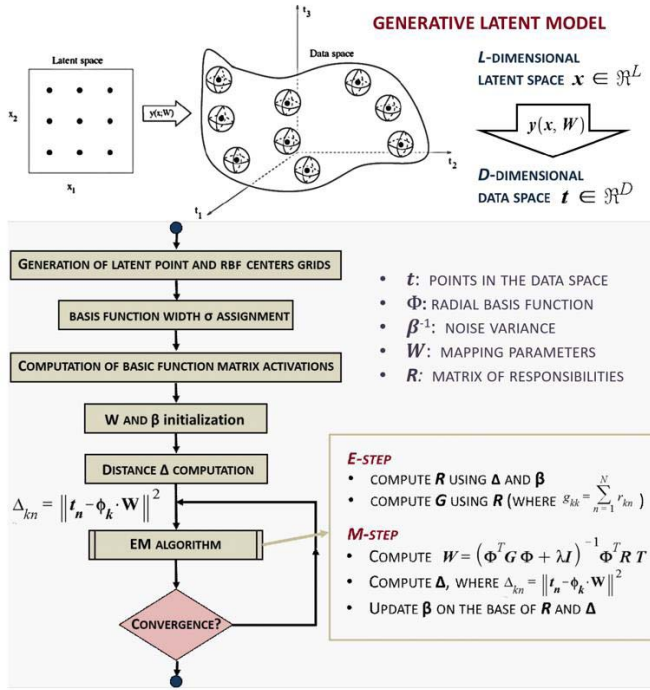


Fig. 9. GTM mapping. The correspondences between a data point in the manifold embedded in the data space and the mean of the posterior distribution in the latent space (top). GTM calculation workflow: the nonlinear mapping (performed through RBFs from a regular grid of latent points to the data space) generates a mixture of Gaussians, whose centers are constrained to lie on a low-D space embedded in the high-D data space (bottom). The defined parametric probability density model is then fitted to the data by maximizing the log likelihood function through the expectation-maximization algorithm [12], [13].

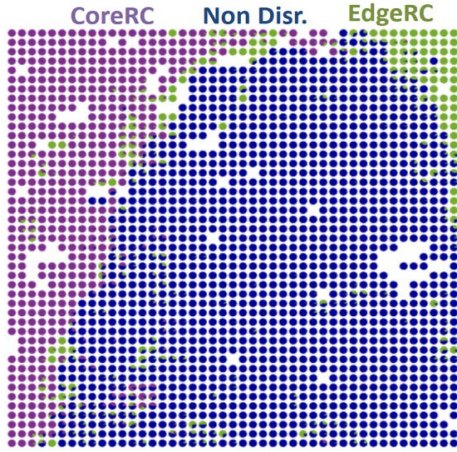


Fig. 10. GTM pie-plane of posterior probability modes. The nondisruptive samples are represented in blue, the samples coming from EdgeRC disruption in light green, and the samples coming from CoreRC disruptions.

nonlinear mapping for the considered data set, which consists of about 110 000 samples for each feature in input as a result of a sampling time of 15 ms for nondisruptive pulses and 5 ms for disruptions unstable phases.

What is particularly interesting to observe is the quite well-defined separation among the three considered classes in the analyzed parameter space.

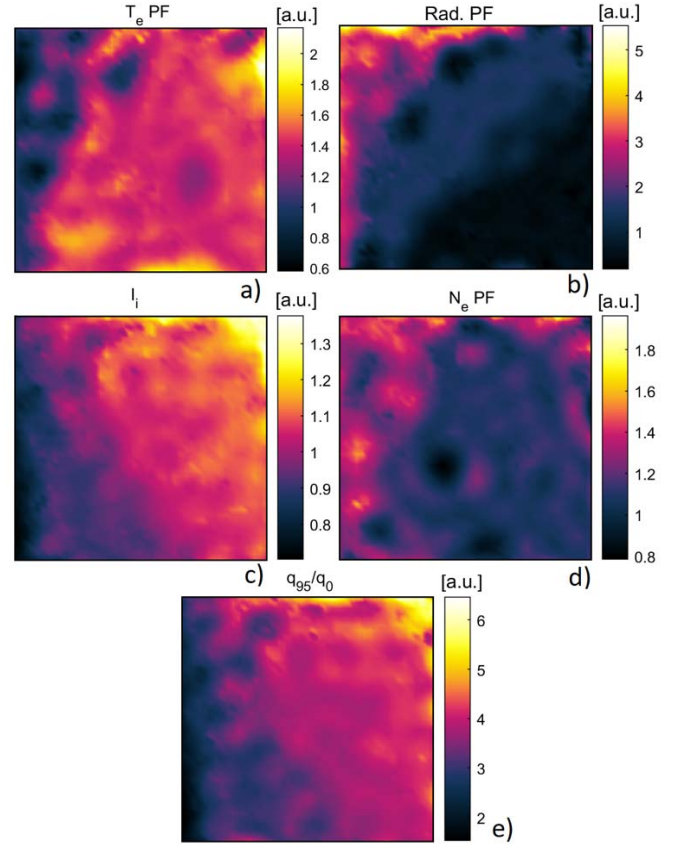


Fig. 11. GTM Component Planes of the of electron temperature peaking factor ( $T_e$ PF), radiation peaking factor (Rad.PF), internal inductance ( $l_i$ ), electron density peaking factor ( $N_e$ PF), and safety factor ratio ( $q_{95}/q_0$ ).

In particular, it is possible to define a boundary separating the region of the operational space dominated by the nondisruptive samples from the regions occupied by the two disruptive classes, where the EdgeRC is located mostly in the top-right corner, whereas the CoreRC class occupies entirely the left side with a broadening in the upper part of the map. While the distribution on the map of the CoreRC class is quite smooth, giving rise to a large, almost continuous area, the EdgeRC distribution is characterized by a slightly larger spread on the map, which can be explained by the significant heterogeneity of the disruption phenomenology composing the EdgeRC group itself.

Another powerful way to visualize data, implemented in the GTM tool previously mentioned, is represented by the component plane analysis, with which it is possible to study characteristic patterns and structures hidden in the high-dimensional data by analyzing the relative component distribution of the input parameters associated with the 2-D mapping.

In Fig. 11, the component planes for all the input parameters have been reported. As can be seen, the distribution of the input parameters shows up all the main features already discussed in Section III dedicated to the univariate analysis, highlighting the combination of the input parameters that provide the separation among the considered classes in the 2-D space. Moreover, it is interesting to note that as expected, the distribution of the internal inductance resembles the  $q_{95}/q_0$

ratio distribution, since they are both strictly related to the peaking of the current density profile. We can also observe that the smoothest distributions are related to the Rad.PF and again to the internal inductance (or the  $q_{95}/q_0$  ratio), where the gradient of the distribution itself changes almost linearly along the diagonal direction (bottom-right corner to top-left corner for the radiation peaking and bottom-left corner to top-right corner for the internal inductance). This is an indication of a lower complexity as far as the contribution of these two parameters to the mapping is concerned. On the contrary, the distribution on the identified manifold for the  $T_e$  and  $N_e$  profile PFs is characterized by a more structured behavior that could be attributed to a not straightforward combination of the considered parameters for specific cases included in the data set. Technically, they depend on the direction of stretching or compression of the 2-D manifold embedded in the 5-D space, that is, required to fit the data.

## V. CONCLUSION

In this paper, PFs for the main plasma profiles have been defined for the JET tokamak with the aim of extracting the information carried out by their evolution in time and have been statistically analyzed for a database with the ILW. The main profiles considered for the analysis are related to the electron temperature ( $T_e$ ), the electron density ( $N_e$ ), the radiation, the ratio  $q_{95}/q_0$ , and finally the internal inductance, intrinsically indicative of the peaking of the plasma current profile itself. Each PF is a “core versus all” metric, i.e., it has been defined as the ratio between the mean value of the considered radial profile around the magnetic axis and the mean value of the measures on the entire radius. The radial interval to define the “core” has been empirically defined as 10% of the radial axis.

Different scenarios have been analyzed discriminating the nondisruptive discharges from the disruptive ones and identifying among this latter two main groups: high-Z impurity accumulation disruptions (already analyzed in [7]), labeled as CoreRC, and disruptions characterized by a final edge radiative cooling, labeled as EdgeRC. These plasma profile-based indicators have been first analyzed by performing a univariate statistical analysis, already showing their high potential in discriminating among the considered classes.

After that the parameter space defined by the considered profiles has been analyzed combining all the features with an advanced manifold learning algorithm, the GTM, highlighting a quite well-defined separation among the class object of the study in the considered parameter space. This result, together with the expected warning times that came out from the analysis, is very promising in the perspective of avoiding and predicting disruptions, which is crucial for JET operations in the upcoming deuterium-tritium campaigns as well as for the design of the ITER plasma control

system. Besides the data analysis/visualization capabilities and the computational efficiency in handling large data sets, the GTM fits into the theoretical framework of probability and statistics, providing the possibility to exploit a well-founded theory to fit models to data, to combine models, to treat incomplete data, etc. This is extremely valuable with regard to the flexibility that is required by a disruption avoidance system and to the integrability in real-time control schemes.

Future work will regard an optimization and a more refined analysis of the defined physics-based parameters, with particular reference to diagnostic data available in real time, and an extension of the analysis to larger databases including further ILW campaigns.

## ACKNOWLEDGMENT

This work has been carried out within the framework of the EUROfusion Consortium. The views and opinions expressed herein do not necessarily reflect those of the European Commission or the ITER Organization, Saint-Paul-lès-Durance, France.

## REFERENCES

- [1] J. Wesson, *Tokamaks*, 2nd ed. Oxford, U.K.: Oxford Univ. Press, 1997, Ch. 3, pp. 105–138.
- [2] P. C. de Vries *et al.*, “Requirements for triggering the ITER disruption mitigation system,” *Fusion Sci. Technol.*, vol. 69, no. 2, pp. 471–484, 2016.
- [3] B. Cannas, A. Fanni, P. Sonato, M. K. Zedda, and EFDA-JET Contributors, “A prediction tool for real-time application in the disruption protection system at JET,” *Nucl. Fusion*, vol. 47, no. 11, p. 1559, 2007.
- [4] G. A. Rattá *et al.*, “An advanced disruption predictor for JET tested in a simulated real-time environment,” *Nucl. Fusion*, vol. 50, no. 2, p. 025005, 2010.
- [5] S. P. Gerhardt *et al.*, “Detection of disruptions in the high- $\beta$  spherical torus NSTX,” *Nucl. Fusion*, vol. 53, no. 6, p. 063021, 2013.
- [6] B. Cannas, A. Fanni, A. Murari, A. Pau, G. Sias, and JET EFDA Contributors, “Overview of manifold learning techniques for the investigation of disruptions on JET,” *Plasma Phys. Controlled Fusion*, vol. 56, no. 11, p. 114005, 2014.
- [7] B. Cannas *et al.*, “Automatic disruption classification in JET with the ITER-like wall,” *Plasma Phys. Controlled Fusion*, vol. 57, p. 125003, Oct. 2015.
- [8] A. Huber *et al.*, “Upgraded bolometer system on JET for improved radiation measurements,” *Fusion Eng. Des.*, vol. 82, pp. 1327–1334, Oct. 2007.
- [9] P. C. de Vries *et al.*, “The influence of an ITER-like wall on disruptions at JET,” *Phys. Plasmas*, vol. 21, p. 056101, Apr. 2014.
- [10] P. C. de Vries *et al.*, “Survey of disruption causes at JET,” *Nucl. Fusion*, vol. 51, no. 5, p. 053018, 2011.
- [11] T. C. Hender *et al.*, “Chapter 3: MHD stability, operational limits and disruptions,” *Nucl. Fusion*, vol. 47, no. 6, p. S128, 2007.
- [12] C. M. Bishop, M. Svensén, and C. K. I. Williams, “GTM: The generative topographic mapping,” *Neural Comput.*, vol. 10, no. 1, pp. 215–234, 1998.
- [13] A. Pau, “Techniques for prediction of disruptions on TOKAMAKS,” Ph.D. dissertation, 2014. [Online]. Available: <http://paduaresearch.cab.unipd.it/6664>

Authors’ photographs and biographies not available at the time of publication.